Post-Annealing Effect on Optical and Electronic Properties of Thermally Evaporated MoOX Thin Films as Hole-Selective Contacts for *p*-Si Solar Cells

Yuanwei Jiang
   Shanghai University School of Materials Science and Engineering

Shuangying Cao
   Chinese Academy of Sciences

Linfeng Lu
   Chinese Academy of Sciences

Guanlin Du
   Chinese Academy of Sciences

Yinyue Lin
   Chinese Academy of Sciences

Jilei Wang
   Jinneng Chean Energy Technology LTD

Liyou Yang
   Jinneng Clean Energy Technology LTD

Wenqing Zhu
   Shanghai University School of Materials Science and Engineering

Dongdong Li (✉ lidd@sari.ac.cn)
   Chinese Academy of Sciences   https://orcid.org/0000-0003-3219-181X

Research Article

Abstract

Owing to its large work function, MoO_X has been widely used for hole-selective contact in both thin film and crystalline silicon solar cells. In this work, thermally evaporated MoO_X films are employed on the rear sides of *p*-type crystalline silicon (*p*-Si) solar cells, where the optical and electronic properties of the MoO_X films as well as the corresponding device performances are investigated as a function of post-annealing treatment. The MoO_X film annealed at 100°C shows the highest work function and proves the best hole selectivity based on the results of energy band simulation and contact resistivity measurements. The full rear *p*-Si/MoO_X/Ag contacted solar cells demonstrate the best performance with an efficiency of 19.19%, which is the result of the combined influence of MoO_X's hole selectivity and passivation ability.

1. Introduction

Transition metal oxides possess a wide range of work functions, spanning from 3.5 eV for defective ZrO_2 to 7.0 eV for stoichiometric V_2O_5 [1-4]. Among them, MoO_X is the most extensively studied for applications in optoelectronic devices [5-7] due to its high transparency in the visible region of the spectrum, nontoxicity and moderate evaporation temperature [8, 9]. MoO_X is reported to have a large work function of ~6.7 eV and is being widely used as hole extraction layers in photovoltaic devices [10], light emitting devices [11], sensors [12, 13] and memories [14]. For photoelectric devices involving MoO_X hole extraction layers, the device performance is strongly dependent on both the optical and electronic properties of the MoO_X thin films. In the photovoltaic field, MoO_X thin films were initially applied in organic devices [15-17]. In recent years, a lot of research has been done on the application of MoO_X films to crystalline silicon (*c*-Si) solar cells [7, 18-20]. By substituting the *p*-type amorphous silicon layer with MoO_X film in the classical silicon heterojunction solar cell, an power conversion efficiency (*PCE*) of 23.5% has been achieved [21]. Compared to MoO_X contacts made to *n*-type wafers, those made to *p*-type wafers (without amorphous Si layer) show better performance in terms of surface passivation and contact resistivity [22]. The feasibility of MoO_X films as hole-selective contacts on *p*-Si solar cells has been demonstrated in our previous work [23], and an efficiency of 20.0% was achieved based on *p*-Si/SiO_X/MoO_X/V_2O_X/ITO/Ag rear contact [24].

MoO_X (X ≤ 3) has a large work function because of the closed shell character in its bulk electronic structure and the dipoles created by its internal layer structure [25]. The presence of oxygen vacancy defects will decrease the work function of MoO_X [4] and result in an *n*-type material [26]. Numerical simulations indicated that higher work function of MoO_X induced a favorable Schottky barrier height as well as an inversion at the MoO_X/intrinsic a-Si:H/*n*-type *c*-Si (*n*-Si) interface, stimulating the path of least resistance for holes [27]. Therefore, tuning the electronic structure and work function of MoO_X is of great significance for solar cells and other similar optoelectronic devices based on silicon substrates with MoO_X contacts.

MoO$_X$ films can be deposited by atomic layer deposition [28-31], reactive sputtering [10], pulsed laser deposition [32], thermal evaporation [22, 33] and spin coating [34], etc. In most of the solar cell researches based on Si/MoO$_X$ contact, MoO$_X$ films are prepared by thermal evaporation at room temperature [6]. Due to the controllability of the properties of MoO$_X$ films by thermal evaporation is limited, various methods of post-treatments were studied to tune the work function of thermally evaporated MoO$_X$. UV-ozone exposure could increase the work function of evaporated MoO$_X$ films on gold substrates from 5.7 eV to 6.6 eV [6]. Irfan et al. performed air annealing of MoO$_X$ films on gold substrates at 300°C for 20 hours, and found that the long-time annealing does not assist in reducing the oxygen vacancies due to the diffusion of gold from substrate towards the MoO$_X$ film [35]. The work function of MoO$_X$ films on p-type c-Si (p-Si) was found to decrease after *in-situ* vacuum annealing in the temperature range from 300 K to 900 K [36].

In this work, p-Si solar cells with MoO$_X$ passivating contacts on rear sides are configured. The optical and electronic properties as well as the influence of the post-annealed MoO$_X$ films on p-Si/MoO$_X$ solar cells are systematically investigated through experiments and energy band simulations. A linear relationship between the work function and the O/Mo atomic ratio is found. It is interesting that, compared with the intrinsic sample, the 100°C-annealed sample with a higher work function exhibits a lower contact resistivity in spite of its thicker SiO$_X$ interlayer. According to the energy band simulation, the variation of MoO$_X$'s work function has little effect on the band bending of p-Si, while the band bending of MoO$_X$ increases significantly as its work function increases. Therefore, it is suggested that higher work functions are vital for effective hole transport from p-Si to MoO$_X$ where the interfacial SiO$_X$ layer is in a moderate thickness range. Our results provide valuable details of the interface characteristics of the p-Si/MoO$_X$ in view of high-performance heterojunction solar cells with oxide-based carrier selective contacts.

2. Methods

Film Deposition, Post Annealing Process and Solar Cell Fabrication

MoO$_X$ films are thermally evaporated at 8 ´ 10^{-4} Pa with a deposition rate of ~0.2 Å/s. Post annealing treatments of the room-temperature-deposited MoO$_X$ films are carried out in a rapid thermal processor in air. The setting temperature was reached in 10 s and held for 5 min. MoO$_X$ films with different annealing temperatures are applied to p-Si solar cells with full rear MoO$_X$/Ag contacts. Detailed process description could be found in our previous work [23]. One difference in cell structure is the implementation of a selective emitter to reduce recombination on the front surface [37].

Measurements

The transmittance spectra of the MoO$_X$ films deposited on 1.2 mm-thick silica glasses are measured using a UV-vis spectrometer with an integrating sphere. Surface morphology and roughness of the films

are measured by atomic force microscope (AFM). The optical properties of the MoO$_X$ films are analyzed using spectroscopic ellipsometry (J.A. Woollam Co., Inc., M2000U ellipsometer) and the measured results are fitted using the native oxide model. High-resolution X-ray photoelectron spectroscopy (XPS) of Mo 3d and Si 2p are measured employing monochromated Al Kα X-rays with a photon energy of 1486.7 eV. The ultraviolet photoemission spectroscopy (UPS) spectra are recorded by using unfiltered He I 21.22 eV excitation with the sample biased at -10 eV. Before XPS and UPS detecting, the surfaces of the samples were pre-cleaned by argon ions. The passivation qualities of MoO$_X$ films with different thickness are determined from effective lifetime measurements *via* quasi-steady state photo conductance (QSSPC) method. The samples for QSSPC test are asymmetric as the front sides are textured, n^+ doped and passivated by means of a double-layered SiN$_X$:H films [38], while the rear sides are covered with the MoO$_X$ films [23]. The current density-voltage characteristics of the solar cells (3.12 × 3.12 cm^2) are measured under standard one sun conditions (100 mW·cm^{-2}, AM1.5G spectrum, 25°C) as the luminous intensity is calibrated with a certified Fraunhofer CalLab reference cell.

Simulations

Numerical simulation of the band structure of the *p*-Si/MoO$_X$ contacts is done with AFORS-HET which is based on solving the one-dimensional Poisson and two carrier continuity equations [39]. The key parameters are listed in Table 1. The front and back contact boundary is set as fixing metal work function to flat band. The interface between *p*-Si and MoO$_X$ is set as "thermionic-emission" (one of the numerical models). Tunneling properties of thin SiO$_2$ film is commonly set by changing the interface parameters under the "thermionic-emission" model only for metal/semiconductor Schottky contact. Therefore, the actually existed tunneling SiO$_X$ at the Si/MoO$_X$ interface is omitted. For *p*-Si, electroneutral defects at the central energy with total trap density is set as 1×10^{14} cm^{-3}. For MoO$_X$, donor-type conduction tail defects with total concentration are set as 1×10^{14} cm^{-3}.

Table 1. Parameters Used for AFORS-HET Simulation.

Parameters	p-Si	MoO$_X$
Later thickness (cm)	1×10^{-4}	1×10^{-6}
Doping concentration (cm^{-3})	1×10^{16} (acceptor)	1×10^{16} - 1×10^{20} (donor)
Relative dielectric constant	11.9	10
Electron affinity (eV)	4.05	6.2
Band gap (eV)	1.124	3.3
Effective conduction band density (cm^{-3})	2.843×10^{19}	1×10^{20}
Effective valence band density (cm^{-3})	2.682×10^{19}	1×10^{20}
Electron mobility (cm^2/Vs)[40]	1107	30
Hole mobility (cm^2/Vs)[40]	424.6	2.5

3. Results And Discussion

Figure 1a represents the photos of the 10-nm-thick MoO$_X$ films on silica glass annealed in air for 5 minutes at different temperatures (100°C, 200°C and 300°C). All of the samples are visually colorless and transparent. From the corresponding optical transmittance spectra in Figure 1b one can see that the transmittance spectrum of the 100°C-annealed MoO$_X$ film almost overlap with that of the unannealed film. Higher annealing temperatures result in a lower transmittance at 600-1100 nm range, which could be assigned to free carrier absorption induced by oxygen vacancies [41]. Thicker MoO$_X$ films (20 nm) are deposited onto polished Si wafers to measure the refractive index n and extinction coefficient k more accurately. The refractive index in Figure 1c lies in the 1.8-2.5 range, which is consistent with other literatures [28, 29]. The n curves as well as the k curves (Figure 1d) have a little difference among the four samples. The n at 633 nm of the 20-nm-thick films decreases slightly, which is summarized in Table 2.

The surface morphologies are then characterized by AFM as shown in Figure S1. The corresponding root mean square (RMS) roughness is listed in Table 2. The as-deposited 10-nm-thick MoO$_X$ thin film (Figure S1a) has an RMS roughness of 4.116 nm, which is in accordance with the wave-like surface morphology. As the annealing temperature goes higher (Figures S1b-d), the surface undulation of the MoO$_X$ film becomes larger while the featured structures become smaller and much denser probably due to the dewetting process [42]. After annealing at 300°C, the RMS roughness reaches 12.913 nm. It is also noted that the 20-nm-thick films are less rough with the RMS around 1 nm (Table 2). The dewetting process is also suppressed as indicated by the RMS measurements as a function of annealing treatments.

Table 2. Root Mean Square Roughness (unit: nm) of 10 nm/20 nm Post-annealed MoO$_X$ Films on SiO$_2$ wafers and Refractive Index n at 633 nm of the 20 nm Films.

Annealing temperature (°C)	None	100°C	200°C	300°C
RMS-10 nm	4.116	8.806	12.124	12.913
RMS-20 nm	1.399	0.940	0.845	0.709
n at 633 nm	1.998	1.997	1.989	1.984

MoO_X has a natural tendency to form oxygen vacancy defects [43], which may impact on the molecular structure. In order to identify such vacancy related molecular structure variations, Raman spectroscopy measurements are conducted on MoO_X(20 nm)/Si(<100>). There are no characteristic peaks of MoO_X in the Raman spectra under green light (532 nm) excitation (Figure S2), which is independent to the thermal treatment. When the excitation is changed to ultraviolet light of 325 nm, characteristic bands of MoO_X appear, which generally locate at 600-1000 cm^{-1} (Figure 2). The sharp peak of 515 cm^{-1} in all samples corresponds to Si-Si bond. For the intrinsic and 100°C-annealed MoO_X films, Raman bands are present at 695, 850 and 965 cm^{-1}, which are from $[Mo_7O_{24}]^{6-}$, $[Mo_8O_{26}]^{4-}$ anions, and $(O=)_2Mo(-O-Si)_2$ dioxo species, respectively [44]. When the film is annealed at 200 °C, the 965 cm^{-1} band shifts to 970 cm^{-1}, which is assigned to $Mo(=^{16}O)_2$ dioxo species [45]. The Raman spectrum of the 300°C-annealed MoO_X film exhibits bands at 695, 810 and 980 cm^{-1}. The band at 810 cm^{-1} is from Si−O−Si bond, while the $(O=)_2Mo(-O-Si)_2$ contributes the band at 980 cm^{-1}. The results indicate that annealing at different temperatures will affect the chemical composition of MoO_X film, which may indicate the difference of oxygen vacancy concentration of each sample.

XPS is conducted on MoO_X films (10 nm) to quantify the relative content of each oxidation state and the oxygen to molybdenum (O/Mo) atomic ratios. After Shirley background subtraction and fitting by Gaussian-Lorentzian curves, a multi-peak deconvolution of the XPS spectra is conducted. The Mo 3d core level is decomposed into two doublet peaks with a doublet spin-orbit splitting Δ_{BE} 3.1 eV and a peak area ratio of 3:2 [9]. As shown in Figure 3, the peak of Mo^{6+} $3d_{5/2}$ core level centers at ~233.3 eV binding energy. For all of the samples, a second doublet at ~232.0 eV, which is denoted as Mo^{5+}, is required to obtain a good fit to the experimental data [6]. The O/Mo ratio is calculated by the following formula [46]:

$$X = \frac{1}{2} \cdot \frac{\sum_n n \cdot I(Mo^{n+})}{\sum_n I(Mo^{n+})}$$

where $I(Mo^{n+})$ is the individual component intensities from the Mo 3d spectra. n relates to the valence state of Mo ion, i.e., 5 for Mo^{5+} and 6 for Mo^{6+}. The factor 1/2 is due to that each oxygen atom is shared by two molybdenum atoms.

The O/Mo ratios of all samples as listed in Table 3 are below 3. Oxygen loss and oxidation state transitions have been reported during transition metal oxides deposition [1]. Since the XPS measurements

are ex-situ, the air exposure to the thermally evaporated MoO_3 films at room temperature could also increase the oxygen vacancies [16, 47]. The O/Mo ratio of the unannealed MoO_X film is 2.958, while post annealing at 100 °C increases the value to 2.964. Higher annealing temperatures then reduce the O/Mo ratio gradually. The highest O/Mo ratio of the 100°C-annealed sample might be explained by the thermally activated oxygen injected from air to the MoO_X film [35]. Figure S3 compares the Si 2p XPS spectra of the 10-nm-thick annealed MoO_X films. The Si 2p XPS spectrum of the unannealed sample shows dual peaks of silicon elements and Si^{4+} peak. A Si^{2+} peak appears when annealed at 100°C. When annealed at 200 and 300°C, peaks of Si^{4+}, Si^{3+} and Si^{2+} exist simultaneously. In addition, the calculated X in SiO_X for the four samples are 2, 1.715, 1.672 and 1.815, respectively. The oxygen atoms in SiO_X are from MoO_X, therefore, the O/Mo ratio depends on the balance between SiOx taking oxygen and air injecting oxygen. By the way, as the annealing temperature goes higher, the signal of Si element becomes weaker, indicating thicker SiO_X interlayers [23].

Table 3. O/Mo Ratio and Work Function of the Post-anealed 10-nm-thick MoO_X Films on Silicon Wafers. Effective Minority Carrier Lifetime of Silicon Wafers Covered by the Post-annealed MoO_X Films.

Annealing temperature (°C)	None	100°C	200°C	300°C	Without MoO_X (Bare Si)
O/Mo ratio	2.958	2.964	2.942	2.957	
Work function (eV)	6.24	6.27	6.21	6.25	
Effective minority carrier lifetime (μs)	26.70	21.53	15.41	9.44	7.76

Reducing the cation oxidation state of an oxide tends to decrease its work function [1]. UPS is utilized to calculate the work function of MoO_X films as a function of thermal treatment. Figure 4a shows the secondary electron cut-off region of the UPS spectra, from which a minor vibration of work function can be seen. From Figure 4b we can see, after post air annealing, the defect peaks in the valence band area [34] become weaker. Table 3 lists the O/Mo ratio evaluated from XPS fitting and corresponding work function evaluated from UPS secondary electron cut-off for samples on polished silicon wafers. The results of the work function and the stoichiometry of MoO_X are also depicted in Figure 4c, where a strong positive correlation is disclosed. An increase of the O/Mo ratio from 2.942 to 2.964 leads to an increase of the work function by roughly 0.06 eV.

Before applying the MoO_X films as passivating contacts on p-Si wafers, one-dimensional energy band simulations are conducted using AFORS-HET [39] to get a clear image of the p-Si/MoO_X heterocontacts. The thicknesses of p-Si and MoO_X film are set as 1 μm and 10 nm, respectively. The acceptor concentration of p-Si is 1×10^{16} cm^{-3}, resulting in a work function of 4.97 eV. Since MoO_X is an n-type

material [48], oxygen vacancies concentration variation is simulated by changing the donor concentration at the range of 1×10^{16} cm^{-3} to 1×10^{20} cm^{-3}. Figure 5a shows that the work function and donor concentration of MoO$_X$ is exponentially correlated. Figure 5c and d depicts the simulated band structure as the donor concentration (N_D) of MoO$_X$ is 1×10^{16} and 1×10^{20} cm^{-3}, respectively. Both the bands of p-Si and MoO$_X$ are bent due to the work function difference and Fermi energy equilibrium. Efficient carrier extraction requires that photogenerated holes in the valence band of p-Si recombine with electrons presented in the MoO$_X$ conduction band that are injected from the adjacent metal electrode [5, 49]. The band bending in p-Si, MoO$_X$ and the total band bending are shown in Figure 5b. As the work function of MoO$_X$ (WF_{MO}) changes, there is no obvious change in the band feature of p-Si. In contrast, the band bending in MoO$_X$, which represents a favorable built-in electric field for electron injection, increases as its work function increases. We can conclude that the increase in the MoO$_X$ work function will raise the total band bending of p-Si/MoO$_X$ contact, most of which lies in the MoO$_X$ part. Therefore, a high work function of MoO$_X$ is desired from the aspect of hole extraction at the p-Si/MoO$_X$ interface.

Figure 6 depicts the dark I-V characteristics of the p-Si/MoO$_X$ contacts using Cox and Stracks method (see Figure S4 for the schematic illustration) [50]. The slope of the I-V curve increases with the increase of the diameter of dot electrode. The I-V curves of the unannealed and 100°C-annealed samples are linear, with the specific contact resistivity (ρ_c) fitted as 0.32 and 0.24 Ω⋅cm^2, respectively. Although annealing at 100°C would make the SiO$_X$ layer at the p-Si/MoO$_X$ interface thicker, the WF_{MO} is higher than that of the unannealed MoO$_X$ film, so the corresponding sample shows the best hole transport characteristic. The I-V curves of the samples annealed at 200 and 300°C become nonlinear at small dot diameter and could not be considered as ohmic contact. Compared with the samples annealed at 100°C, samples annealed at higher annealing temperatures possess lower currents. As the small drop of work function, the main reason would be that higher annealing temperature causes thicker SiO$_X$ layer at the p-Si/MoO$_X$ interface, making it more difficult for carriers to tunnel through the oxide barrier.

The passivation qualities of the MoO$_X$(10 nm)/p-Si heterojunctions as a function of thermal treatment are characterized in terms of effective minority carrier lifetime (τ_{eff}). The injection-level-dependent τ_{eff}s are shown in Figure S5, where the τ_{eff}s at an injection level of 1×10^{15} cm^{-3} are listed in Table 3. The unannealed MoO$_X$ film shows the best passivation ability. Higher treating temperature leads to lower τ_{eff}, which is the combined result of the chemical passivation of the interfacial SiO$_X$ and the field effect passivation of MoO$_X$, as larger X in SiO$_X$ means fewer dangling bonds of silicon and larger X in MoO$_X$ means larger built-in electric field intensity.

The MoO$_X$ films are then adopted into the p-Si/MoO$_X$(10 nm)/Ag configuration (Figure 7a) to investigate the influence of MoO$_X$'s electronic properties on the device performance. The light current density versus voltage (J-V) curves are shown in Figure 7b. The average J-V characteristics are shown in Figure 7c-f. The lower V_{OC}s after annealing are in line with the lower τ_{eff}. All cells, except for the ones with MoO$_X$ annealed

at 300°C, share similar J_{SC} (~38.8 mA/cm^2), which means the minor difference in optical index of MoO$_X$ and variation in the thickness of the interfacial SiO$_X$ have little influence in the effective optical absorption of bulk silicon at long wavelength range. The best PCE of solar cells with unannealed MoO$_X$ films is 18.99%, which is similar to our previous report [23]. A PCE of 19.19% is achieved when 100°C annealing is applied. The PCE improvement mainly comes from the elevated fill factor (FF) with reduced series resistance, as demonstrated by the low contact resistance in Figure 6b. Inefficient transport of holes leads to the decrease of FF, which is prominent on the devices with 300°C annealing. Higher annealing temperature leads to PCE drop that is originated from reduced V_{OC} (degraded field effect passivation of MoO$_X$) and FF (thicker SiO$_X$ interlayer reduces the carrier tunneling probability).

Overall, the performance of the p-Si/MoO$_X$ heterojunction solar cell is affected by the passivation quality, work function and band-to-band tunneling [31] properties of the hole-selective MoO$_X$ film. The passivation performance of the present structure is still poor, leading to relatively lower V_{OC}. Therefore, efficient surface passivation will be a research focus for non-doped carrier selective contacts.

4. Conclusions

In summary, MoO$_X$ films with different oxygen vacancy concentrations were obtained by post annealing at different temperatures. The O/Mo atomic ratio of MoO$_X$ films is linearly related to their work function. Compared with the intrinsic MoO$_X$ film, the one annealed at 100°C obtained less oxygen vacancy and higher work function. Energy band simulation shows that the band bending of p-Si in the p-Si/MoO$_X$ contact is basically the same when the work function of MoO$_X$ varies from 6.20 eV to 6.44 eV. Nevertheless, a larger work function yields increased band bending in MoO$_X$ film. Experimental results indicate that the moderately improved work function of MoO$_X$ annealed at 100°C is favorable for hole selectivity. The corresponding solar cell with optimized full rear p-Si/MoO$_X$/Ag contact achieved a PCE of 19.19%.

Abbreviations

c-Si: Crystalline silicon

p-Si: *p*-type crystalline silicon

n-Si: *n*-type *c*-Si

PCE: Power conversion efficiency

AFM: Atomic force microscope

XPS: X-ray photoelectron spectroscopy

UPS: Ultraviolet photoemission spectroscopy

QSSPC: Quasi-steady state photo conductance

RMS: Root mean square

WF: Work function

FF: Fill factor

Declarations

Availability of data and material

The datasets used and analyzed during the current study are available from the corresponding author on reasonable request.

Competing interests

The authors declare that they have no competing interests.

Funding

Authors contributions

DL and WZ provided the idea and experimental design of this study. SC and GD deposited the materials and prepared the devices. YJ and YL wrote the manuscript. All author discussed the results and commented on the manuscript. All authors read and approved the final manuscript.

Acknowledgements

References

1. M. T. Greiner and Z.-H. Lu (2013) Thin-film metal oxides in organic semiconductor devices: their electronic structures, work functions and interfaces. *NPG Asia Mate* 5(7): e55
2. J. Bullock, Y. Wan, Z. Xu, S. Essig, and A. Javey (2018) Stable Dopant-free Asymmetric Heterocontact Silicon Solar Cells with Efficiencies Above 20%. *ACS Energy Lett* 3(3): 508-513

3. Y. Wan, S. K. Karuturi, C. Samundsett, J. Bullock, M. Hettick, D. Yan, J. Peng, P. R. Narangari, S. Mokkapati, and H. H. Tan (2018) Tantalum Oxide Electron-selective Heterocontacts for Silicon Photovoltaics and Photoelectrochemical Water Reduction. *ACS Energy Lett* 3(1):125-131

4. M. T. Greiner, L. Chai, M. G. Helander, W.-M. Tang, and Z.-H. Lu (2012) Transition Metal Oxide Work Functions: The Influence of Cation Oxidation State and Oxygen Vacancies. *Adv Funct Mater* 22(21): 4557-4568

5. C. Battaglia, S. M. De Nicolas, S. De Wolf, X. Yin, M. Zheng, C. Ballif, and A. Javey (2014) Silicon heterojunction solar cell with passivated hole selective MoOx contact. *Appl Phys Lett* 104(11): 113902

6. C. Battaglia, X. Yin, M. Zheng, I. D. Sharp, T. Chen, S. McDonnell, A. Azcatl, C. Carraro, B. Ma, R. Maboudian, R. M. Wallace, and A. Javey (2014) Hole selective MoO_x contact for silicon solar cells. *Nano Lett* 14(2): 967-71

7. J. Bullock, M. Hettick, J. Geissbühler, A. J. Ong, T. Allen, Carolin M. Sutter-Fella, T. Chen, H. Ota, E. W. Schaler, S. De Wolf, C. Ballif, A. Cuevas, and A. Javey (2016) Efficient silicon solar cells with dopant-free asymmetric heterocontacts. *Nat Energy* 1(3): 15031

8. J. Meyer and A. Kahn (2011) Electronic structure of molybdenum-oxide films and associated charge injection mechanisms in organic devices. *J Photonics Energy* 1(1): 011109

9. L. G. Gerling, S. Mahato, A. Morales-Vilches, G. Masmitja, P. Ortega, C. Voz, R. Alcubilla, and J. Puigdollers (2016) Transition metal oxides as hole-selective contacts in silicon heterojunctions solar cells. *Sol. Energy Mater Sol Cells* 145: 109-115

10. A. L. F. Cauduro, R. dos Reis, G. Chen, A. K. Schmid, C. Méthivier, H.-G. Rubahn, L. Bossard-Giannesini, H. Cruguel, N. Witkowski, and M. Madsen (2017) Crystalline Molybdenum Oxide Thin-Films for Application as Interfacial Layers in Optoelectronic Devices. *ACS Appl Mater Interfaces* 9(8): 7717-7724

11. F. Wang, X. Qiao, T. Xiong, and D. Ma (2008) The role of molybdenum oxide as anode interfacial modification in the improvement of efficiency and stability in organic light-emitting diodes. *Org Electron* 9(6): 985-993

12. M. D. Giulio, D. Manno, G. Micocci, A. Serra, and A. Tepore (1998) Physical Properties of Molybdenum Oxide Thin Films for NO Gas Detection. *Phys Status Solidi A* 168(1): 249-256

13. M. M. Y. a. Alsaif, M. R. Field, B. J. Murdoch, T. Daeneke, K. Latham, A. F. Chrimes, A. S. Zoolfakar, S. P. Russo, J. Z. Ou, and K. Kalantar-zadeh (2014) Substoichiometric two-dimensional molybdenum oxide flakes: a plasmonic gas sensing platform. *Nanoscale* 6(21): 12780-12791

14. A. A. Bessonov, M. N. Kirikova, D. I. Petukhov, M. Allen, T. Ryhänen, and M. J. A. Bailey (2015) Layered memristive and memcapacitive switches for printable electronics. *Nat Mater* 14(2): 199-204

15. M. Vasilopoulou, A. M. Douvas, D. G. Georgiadou, L. C. Palilis, S. Kennou, L. Sygellou, A. Soultati, I. Kostis, G. Papadimitropoulos, and D. Davazoglou (2012) The Influence of Hydrogenation and Oxygen Vacancies on Molybdenum Oxides Work Function and Gap States for Application in Organic Optoelectronics. *J Amer Chem Soc* 134(39): 16178-16187

16. Irfan, H. Ding, Y. Gao, D. Y. Kim, J. Subbiah, and F. So (2010) Energy level evolution of molybdenum trioxide interlayer between indium tin oxide and organic semiconductor. *Appl Phys Lett* 96(7): 073304

17. S. Chambon, L. Derue, M. Lahaye, B. Pavageau, L. Hirsch, and G. Wantz (2012) MoO_3 Thickness, Thermal Annealing and Solvent Annealing Effects on Inverted and Direct Polymer Photovoltaic Solar Cells. *Mater* 5(12): 2521-2536

18. L. Neusel, M. Bivour, and M. Hermle (2017) Selectivity issues of MoO_x based hole contacts. *Energy Procedia* 124: 425-434

19. T. Sun, R. Wang, R. Liu, C. Wu, Y. Zhong, Y. Liu, Y. Wang, Y. Han, Z. Xia, and Y. Zou (2017) Investigation of MoO_x/n-Si strong inversion layer interfaces via dopant-free heterocontact. *Physica Status Solidi Rapid Research Letters* 11(7): 1700107

20. D. Sacchetto, Q. Jeangros, G. Christmann, L. Barraud, A. Descoeudres, J. Geissbühler, M. Despeisse, A. Hessler-Wyser, S. Nicolay, and C. Ballif (2017) ITO/MoO_x/a-Si:H(i) Hole-Selective Contacts for Silicon Heterojunction Solar Cells: Degradation Mechanisms and Cell Integration. *IEEE J Photovoltaics* 7(6): 1584-1590

21. J. Dréon, Q. Jeangros, J. Cattin, J. Haschke, L. Antognini, C. eBallif, and M. Boccard (2020) 23.5%-efficient silicon heterojunction silicon solar cell using molybdenum oxide as hole-selective contact. *Nano Energy* 70: 104495

22. J. Bullock, A. Cuevas, T. Allen, and C. Battaglia (2014) Molybdenum oxide MoO_x: A versatile hole contact for silicon solar cells. *Appl Phys Lett* 105(23): 232109

23. S. Cao, J. Li, Y. Lin, T. Pan, G. Du, J. Zhang, X. Chen, l. Lu, N. Min, M. Yin, and D. Li (2019) Interfacial Behavior and Stability Analysis of p-type Crystalline Silicon Solar Cells Based on Hole-selective MoO_x/Metal Contacts. *Solar RRL* 3(11): 1900274

24. S. Cao, J. Li, J. Zhang, Y. Lin, L. Lu, J. Wang, M. Yin, L. Yang, X. Chen, and D. Li (2020) Stable MoO_x-based Heterocontacts for p-type Crystalline Silicon Solar Cells Achieving 20% Efficiency. *Adv Funct Mater* 30(49): 2004367

25. Y. Guo and J. Robertson (2014) Origin of the high work function and high conductivity of MoO_3. *Appl Phys Lett* 105(22): 222110

26. M. T. Greiner, M. G. Helander, W.-M. Tang, Z.-B. Wang, J. Qiu, and Z.-H. Lu (2012) Universal energy-level alignment of molecules on metal oxides. *Nat Mater* 11(1): 76-81

27. H. Mehmood, H. Nasser, T. Tauqeer, S. Hussain, E. Ozkol, and R. i. Turan (2017) Simulation of an efficient silicon heterostructure solar cell concept featuring molybdenum oxide carrier-selective contact. *Int J Energy Res* 42(4): 1-17

28. B. Macco, M. F. J. Vos, N. F. W. Thissen, A. A. Bol, and W. M. M. Kessels (2015) Low-temperature atomic layer deposition of MoO_x for silicon heterojunction solar cells. *Physica Status Solidi Rapid Research Letters* 9(7): 393-396

29. M. F. J. Vos, B. Macco, N. F. W. Thissen, A. A. Bol, and W. M. M. Kessels (2016) Atomic layer deposition of molybdenum oxide from $(NtBu)_2(NMe_2)_2Mo$ and O_2 plasma. *J Vacuum Sci Tech A Vacuum Surfaces Films* 34(1): 01A103

30. J. Ziegler, M. Mews, K. Kaufmann, T. Schneider, A. N. Sprafke, L. Korte, and R. B. Wehrspohn (2015) Plasma-enhanced atomic-layer-deposited MoO_x emitters for silicon heterojunction solar cells. *Appl Phys A* 120(3): 811-816

31. T. P. Jingye Li, Jilei Wang, Shuangying Cao, Yinyue Lin, Bram Hoex, Zhongquan Ma, Linfeng Lu, Liyou Yang, Baoquan Sun, Dongdong Li (2020) Bilayer MoO_x/CrO_x Passivating Contact Targeting High Stable Silicon Heterojunction Solar Cell. *ACS Appl Mater Interfaces* 12(32): 36778-36786

32. K. Inzani, M. Nematollahi, F. Vullum-Bruer, T. Grande, T. W. Reenaas, and S. M. Selbach (2017) Electronic properties of reduced molybdenum oxides. *Phys Chem Chem Phys* 19(13): 9232-9245

33. H.-D. Um, N. Kim, K. Lee, I. Hwang, J. H. Seo, and K. Seo (2016) Dopant-Free All-Back-Contact Si Nanohole Solar Cells Using MoO_x and LiF Films. *Nano Lett* 16(2): 981-987

34. J. Tong, Y. Wan, J. Cui, S. Lim, N. Song, and A. Lennon (2017) Solution-processed Molybdenum Oxide for Hole-selective Contacts on Crystalline Silicon Solar Cells. *Appl Surf Sci* 423: 139-146

35. I. Irfan and Y. Gao (2012) Effects of exposure and air annealing on MoO_x thin films. *J Photonics Energy* 2(1): 021213

36. T. Zhang, C.-Y. Lee, Y. Wan, S. Lim, and B. Hoex (2018) Investigation of the thermal stability of MoO_x as hole-selective contacts for Si solar cells. *J Appl Phys* 124(7): 073106

37. J. Supawan, K. Yasuhiro, M. Masaaki, U. Satoshi, S. Katsuhiko, and T. Hidetaka (2018) Assisted passivation by a chemically grown SiO_2 layer for *p*-type selective emitter-passivated emitter and rear cells. *Sol Energy Mater Sol Cells* 186: 84-91

38. J. Ko, D. Gong, K. Pillai, K. S. Lee, and B. Choi (2011) Double layer SiN_x:H films for passivation and anti-reflection coating of cSi solar cells. *Thin Solid Films* 519(20): 6887-6891

39. R. Varache, C. Leendertz, M. E. Gueunier-Farret, J. Haschke, and L. Korte (2015) Investigation of selective junctions using a newly developed tunnel current model for solar cell applications. *Sol Energy Mater Sol Cells* 141: 14-23

40. L.-C. Hao, M. Zhang, M. Ni, J.-M. Liu, and X.-D. Feng (2018) Simulation of high efficiency silicon heterojunction solar cells with molybdenum oxide carrier selective layer. *Mater Res Express* 5(7): 075504

41. W. Wang, H. Peelaers, J.-X. Shen, and C. G. Van de Walle (2018) Carrier-induced absorption as a mechanism for electrochromism in tungsten trioxide. *MRS Communications* 8(3): 926-931

42. C. V. Thompson (2012) Solid-state dewetting of thin films. *Annual Review of Materials Research* 42: 399-434

43. J. Meyer, A. Shu, M. Kröger, and A. Kahn (2010) Effect of contamination on the electronic structure and hole-injection properties of MoO_3/organic semiconductor interfaces. *Appl Phys Lett* 96(13): 133308

44. I. E. Wachs and C. A. Roberts (2010) Monitoring surface metal oxide catalytic active sites with Raman spectroscopy. *Chem Soc Rev* 39: 5002–5017

45. E. L. Lee and I. E. Wachs (2008) In Situ Raman Spectroscopy of SiO_2-Supported Transition Metal Oxide Catalysts: An Isotopic ^{18}O-^{16}O Exchange Study. *Journal of Physical Chemistry C* 112(16): 6487-6498

46. F. G. Bell and L. Ley (1988) Photoemission study of SiO_x ($0 \leq x \leq 2$) alloys. *Physical Review B* 37(14): 8383

47. K. Kanai, K. Koizumi, S. Ouchi, Y. Tsukamoto, K. Sakanoue, Y. Ouchi, and K. Seki (2010) Electronic structure of anode interface with molybdenum oxide buffer layer. *Org Electron* 11(2): 188-194

48. M. Kröger, S. Hamwi, J. Meyer, T. Riedl, and W. Kowalsky (2009) Role of the deep-lying electronic states of MoO_3 in the enhancement of hole-injection in organic thin films. *Appl Phys Lett* 95(12): 123301

49. S. Essig, J. Dréon, E. Rucavado, M. Mews, and C. Balllif (2018) Toward Annealing-Stable Molybdenum-Oxide-Based Hole-Selective Contacts For Silicon Photovoltaics. *Solar RRL* 2(4): 1700227

50. R. H. Cox and H. Strack (1967) Ohmic contacts for GaAs devices. *Solid State Electronics* 10: 1213–1218

Supplementary Information

Figure S1. Atomic force microscopy images of the MoO_x thin films at different post annealing temperatures. **Figure S2.** Green light (532 nm) Raman scattering intensity of polished Si surface and MoO_x films. **Figure S3.** Si 2p XPS spectra of the MoO_x films on Si wafers at different post annealing temperatures. **Figure S4.** Schematic diagram of the test sample, electrode contact pattern, and test circuit for a specific contact resistivity measurement. **Figure S5.** Injection-level-dependent effective minority carrier lifetime of bare Si and MoO_x films at different post annealing temperatures.
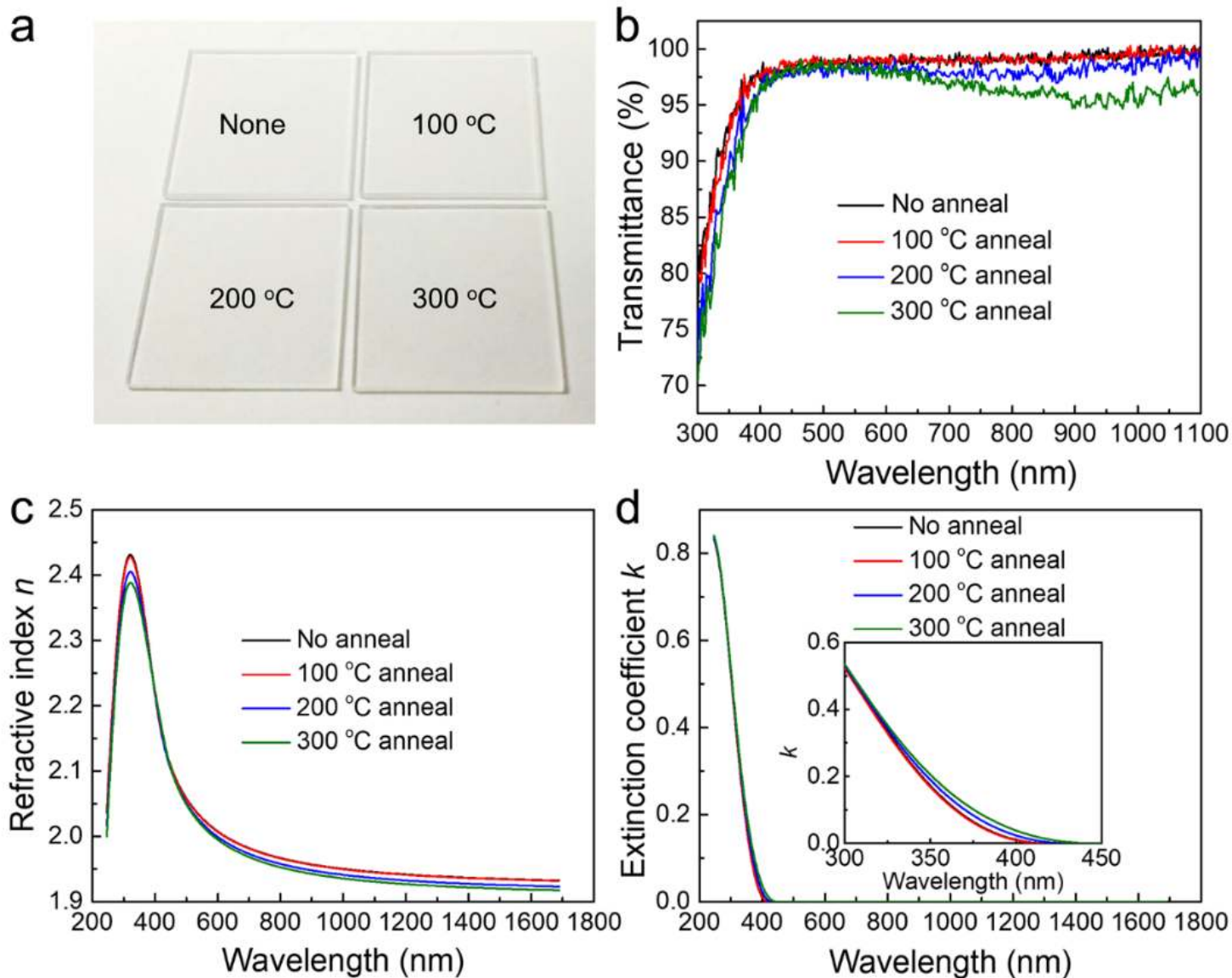
Figures

Figure 1

(a) Photos and (b) transmittance spectra of the 10-nm-thick MoOX films on silica glass annealed in air for 5 minutes at different temperatures. (c) Refractive indices n and (d) extinction coefficient k curves of the 20-nm-thick MoOX films on polished silicon wafers.
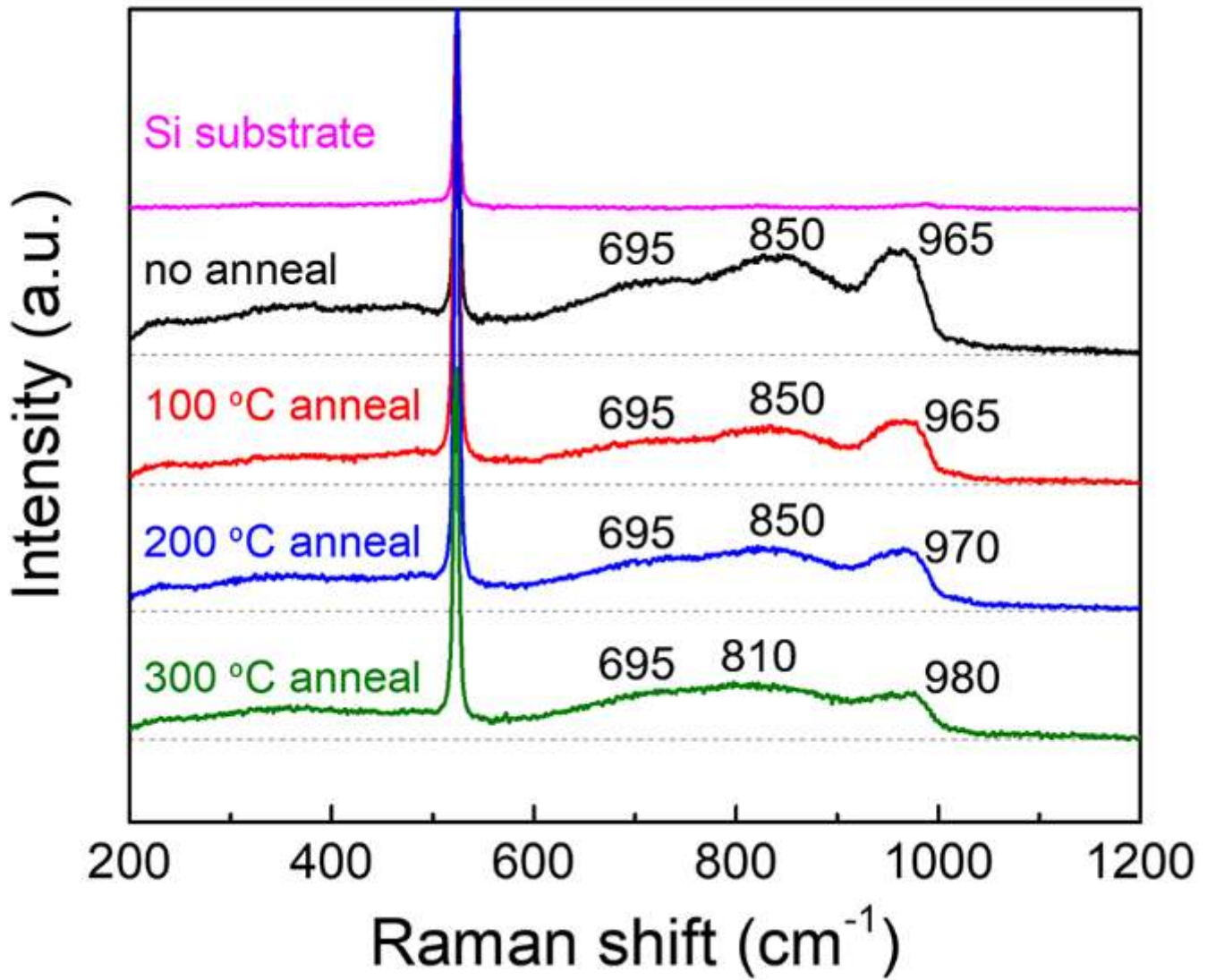
Figure 2

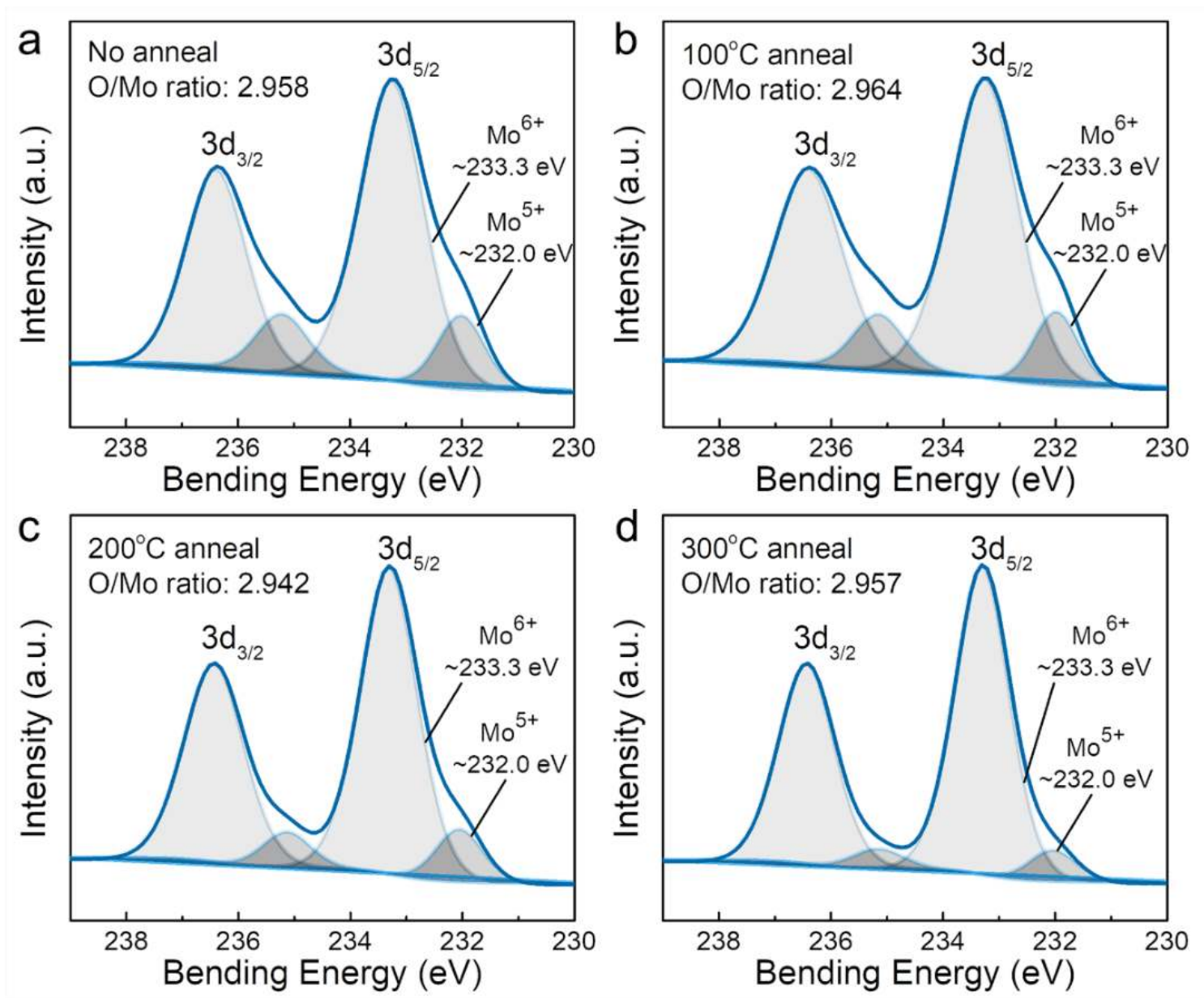The UV Raman (325 nm) spectra of post-annealed 20-nm-thick MoOX films on polished silicon wafers.

Figure 3

Mo 3d core level XPS spectra of the 10-nm-thick MoOX films on silicon wafers (a) without post annealing, with post annealing at (b) 100oC, (c) 200oC and (d) 300oC.
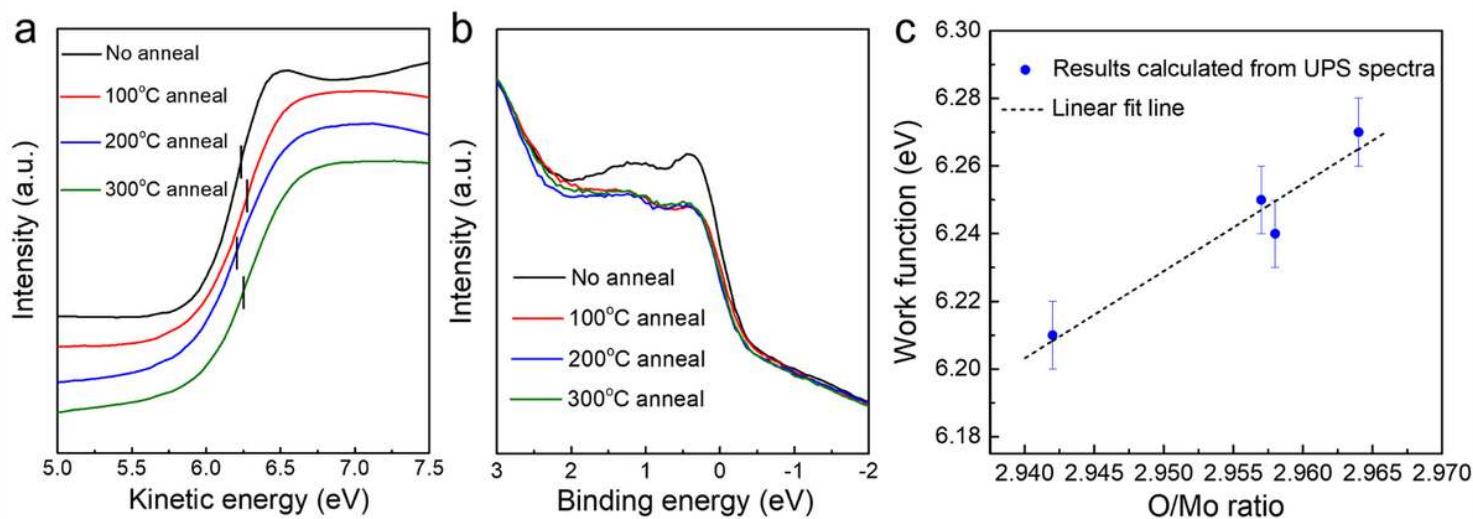
Figure 4

(a) The secondary electron cut-off region and (b) valence band from the UPS spectra of the post-annealed MoOX films on silicon wafers. (c) Work function plotted against the stoichiometry (O/Mo ratio).
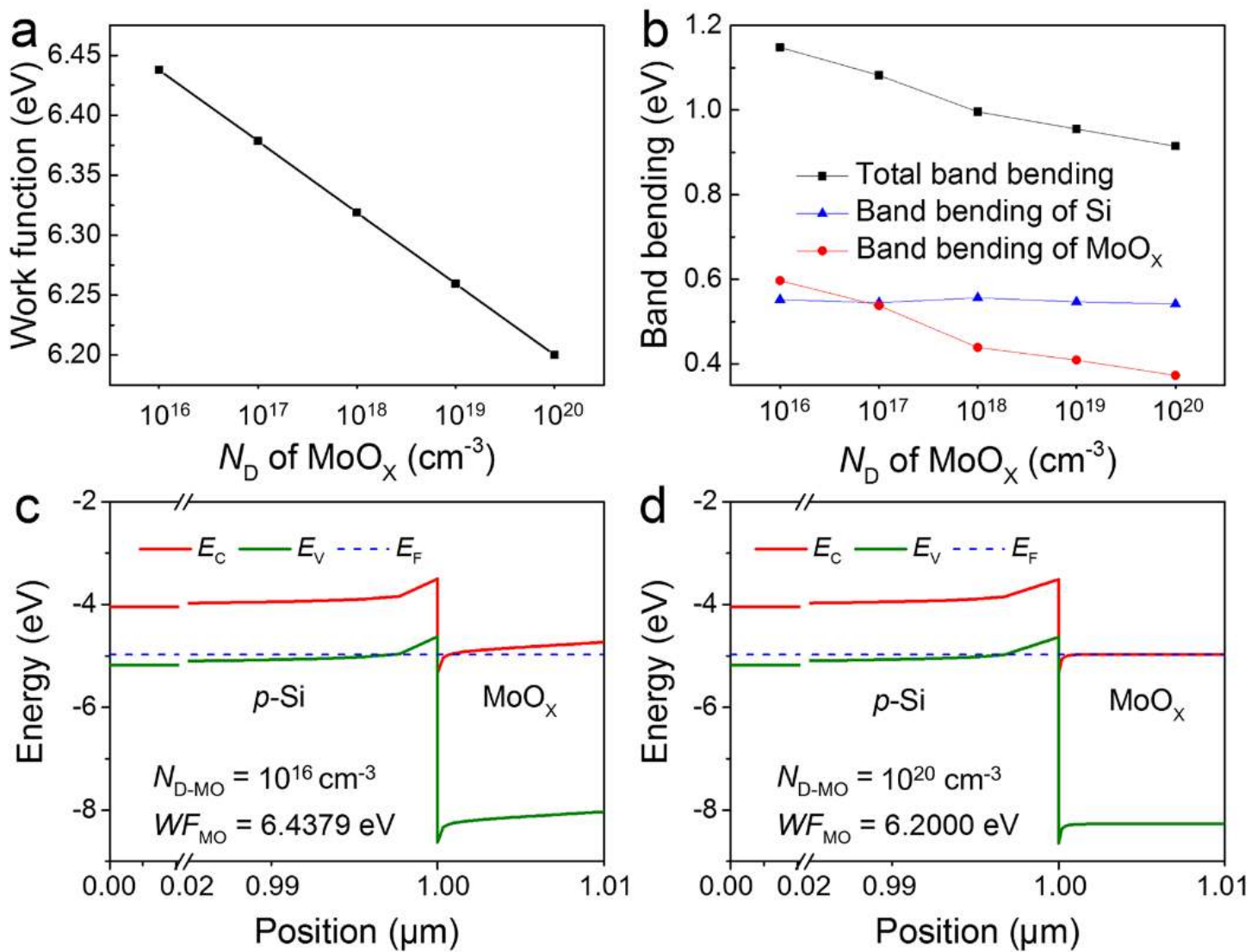
Figure 5

Simulated energy band results of the p-Si/MoOX contact. (a) The relationship between the work function and ND of MoOX (ND-MO). (b) The p-Si, MoOX and the total band bending for p-Si/MoOX contact. The acceptor concentration of p-Si is 1×10^{16} cm-3. Simulated band diagrams of p-Si/MoOX contact as the ND-MO is (c) 1×10^{16} cm-3 and (d) 1×10^{20} cm-3, respectively.
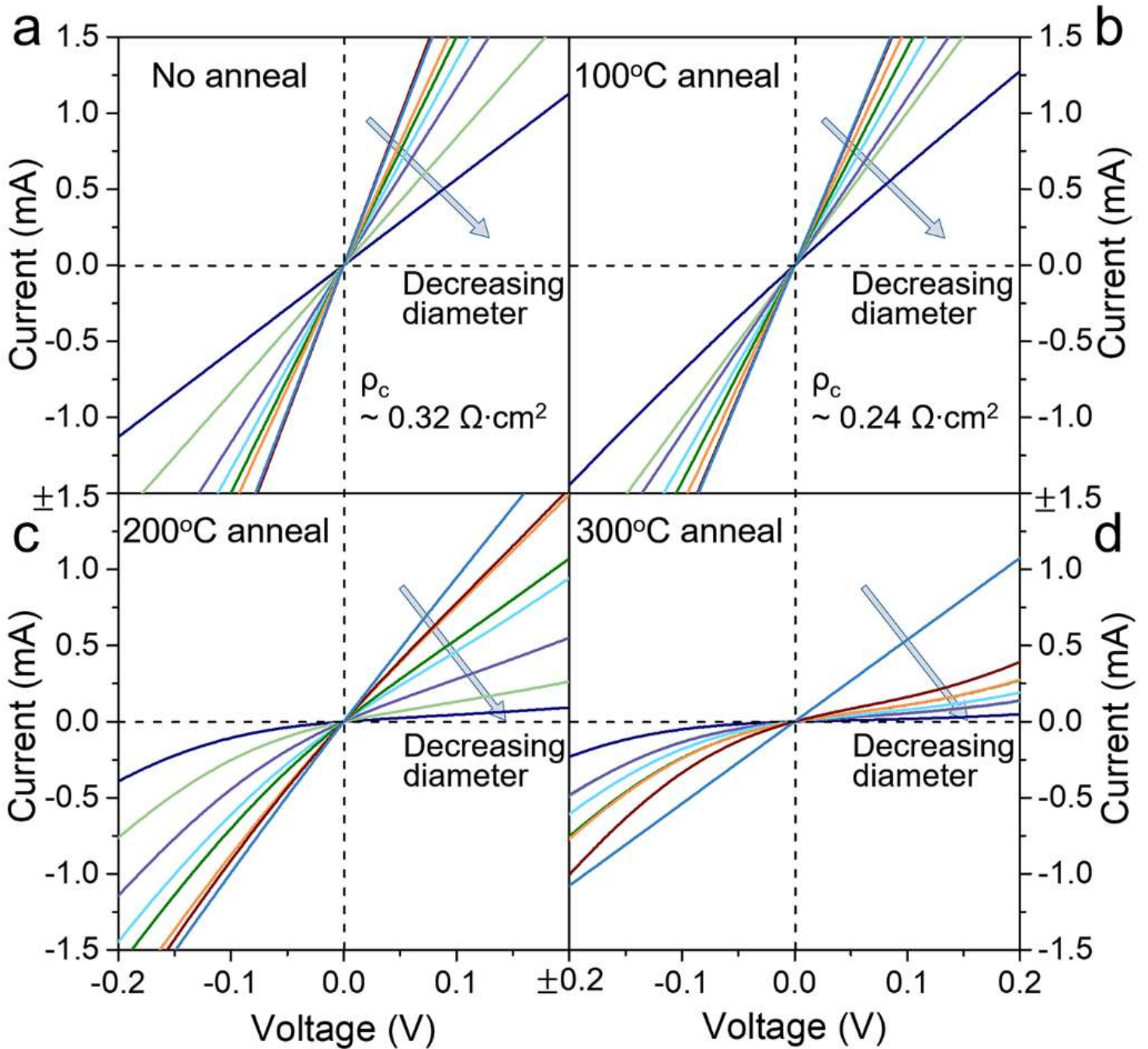

Figure 6

Contact resistance measurements of the 10-nm-thick MoOX films on polished silicon wafers (a) without post annealing, with post annealing at (b) 100oC, (c) 200oC and (d) 300oC.
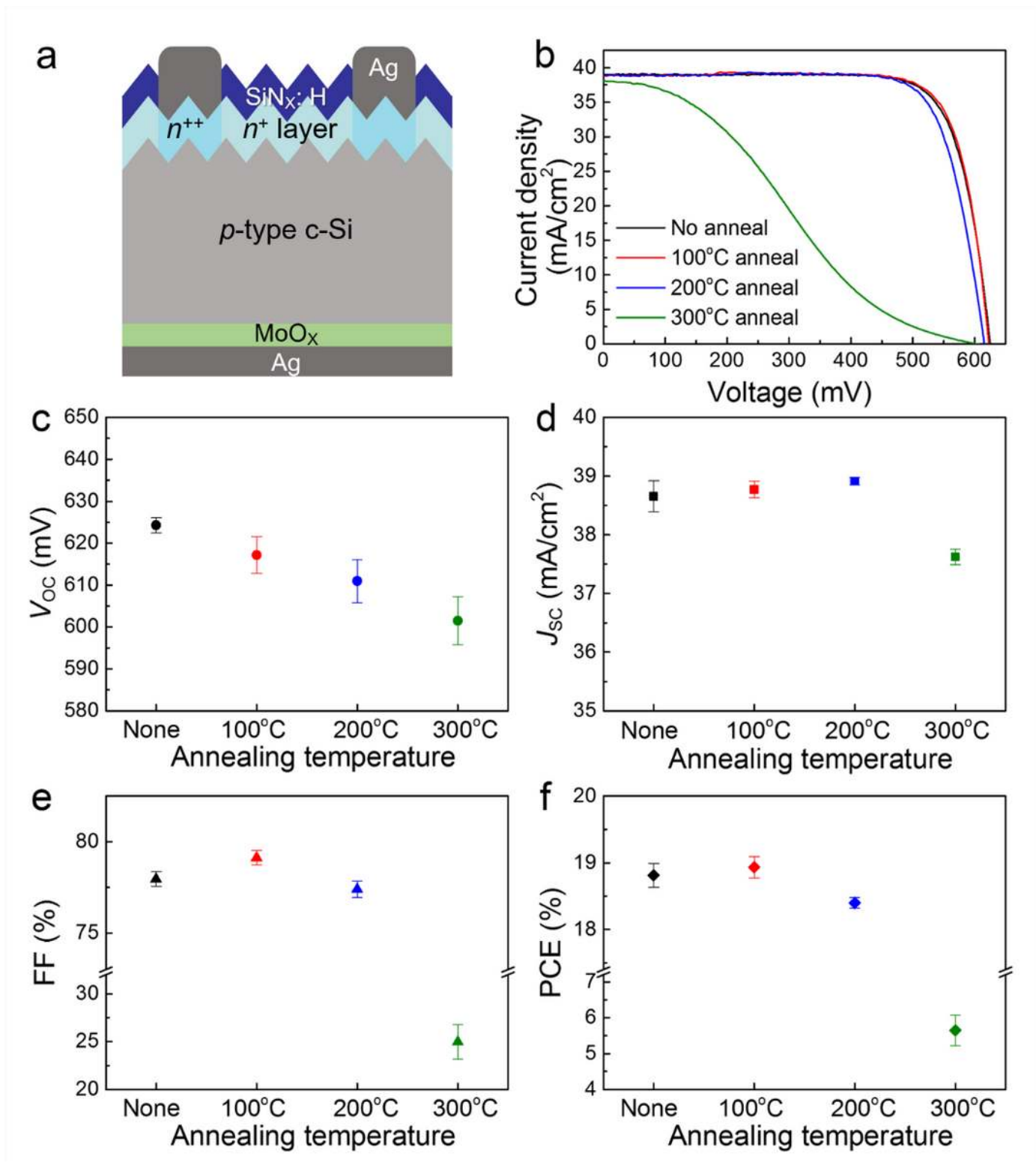
Figure 7

(a) Cross-sectional schematic, (b) J-V curves and (c-f) average J-V parameters of the p-Si/MoOX/Ag solar cells with MoOX films annealed at different temperatures.

Supplementary Files

This is a list of supplementary files associated with this preprint. Click to download.

- SupplementaryInformation.docx